

**Theoretical investigation on the energy absorption of ellipse-shaped self-locked tubes**

[Yang Kuijian](#), [Qiao Chuan](#), [Xiong Feng](#), [Zhang Lei](#), [Wu Zhangming](#) and [Chen Yuli](#)

Citation: [SCIENCE CHINA Physics, Mechanics & Astronomy](#); doi: 10.1007/s11433-019-1518-9

View online: <http://engine.scichina.com/doi/10.1007/s11433-019-1518-9>

Published by the [Science China Press](#)

---

**Articles you may be interested in**

[Molecular design and theoretical investigation into one- and two-photon absorption properties of two series of cyclometalated platinum \(II\) complexes](#)

SCIENCE CHINA Chemistry **55**, 1405 (2012);

[Theoretical study of electric energy consumption for self-powered chaos signal generator](#)

SCIENCE CHINA Technological Sciences **57**, 1063 (2014);

[Pulses compression in a self-mode-locked Ti:sapphire laser](#)

Chinese Science Bulletin **41**, 723 (1996);

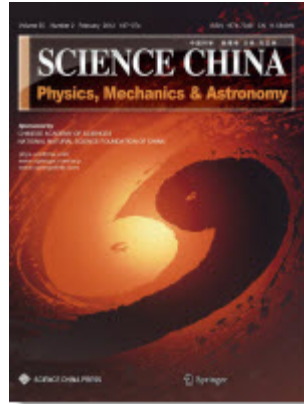
[Investigation and performance evaluation of optically thin laser-induced breakdown spectroscopy without self-absorption](#)

SCIENTIA SINICA Physica, Mechanica & Astronomica **47**, 124201 (2017);

[Investigation and characterization of an arc-shaped piezoelectric generator](#)

SCIENCE CHINA Technological Sciences **56**, 2636 (2013);

---



### Theoretical investigation on the energy absorption of ellipse-shaped self-locked tubes

Journal:	<i>SCIENCE CHINA Physics, Mechanics &amp; Astronomy</i>
Manuscript ID	SCPA-2019-0538.R2
Manuscript Type:	Original Article
Date Submitted by the Author:	22-Jan-2020
Complete List of Authors:	Yang, Kuijian Qiao, Chuan Xiong, Feng Zhang, Lei Wu, Zhangming Chen, Yuli
Keywords:	Energy absorption, Ellipse-shaped self-lock tube, Plastic hinge model, Thin-walled structure
Speciality:	Solid Mechanics

SCHOLARONE™  
Manuscripts

# Theoretical investigation on the energy absorption of ellipse-shaped self-locked tubes

Kuijian Yang<sup>1,#</sup>, Chuan Qiao<sup>2,#</sup>, Feng Xiong<sup>1</sup>, Lei Zhang<sup>1</sup>, Zhangming Wu<sup>3</sup>,

Yuli Chen<sup>1,\*</sup>

<sup>1</sup>Institute of Solid Mechanics, Beihang University, Beijing 100191, China

<sup>2</sup>Department of Mechanical Engineering, McGill University, Montreal, QC H3A0C3, Canada

<sup>3</sup>Cardiff School of Engineering, Queens Buildings, The Parade, Newport Road, Cardiff CF24 3AA, UK

#These authors contributed equally to this work.

\* To whom correspondence may be addressed: yulicheng@buaa.edu.cn

## Abstract

Self-locked energy-absorbing systems have been proposed in previous studies to overcome the limitations associated with the round-tube systems because they can prevent the lateral splash of tubes from impact loadings without any constraints. In case of self-locked systems, the ellipse-shaped self-locked tube is considered to be an optimal design when compared with the ordinary circle-shaped self-locked tubes and other shaped self-locked tubes. In this study, we aim to theoretically analyze the ellipse-shaped self-locked tubes. Further, a plastic hinge model is developed to predict the force–displacement relation of the tube, which is compared with the deformation process observed in the experiment and finite element method (FEM) simulation. Using this model, the effects of tuning the geometric parameters of the tube on the energy absorption performance, including the deformation efficiency, energy absorption capacity, and effective stroke ratio, are simulated and analyzed. Finally, a

1  
2  
3 guideline is provided with respect to the design of the ellipse-shaped self-locked tube  
4  
5  
6 in engineering applications.  
7  
8  
9

## 10 **1. Introduction**

11  
12 Sudden impacts and blast loadings considerably damage lives and properties  
13  
14 owing to their destructiveness and unpredictability. Therefore, the development of  
15  
16 effective energy absorption devices plays a paramount role in many fields, including  
17  
18 aerospace, navigation, and road traffic [1-6]. The metallic thin-walled round-tube  
19  
20 system is one of the most widely used energy absorption devices for impact protection  
21  
22 owing to its low cost, manufacturability, and high specific energy absorption [7-10].  
23  
24 Recently, researchers have focused on improving the energy absorption properties of  
25  
26 the round-tube system by designing novel shapes and geometry for tubes, including  
27  
28 square, elliptical, spherical, and tapered shells [11-16]. Some researchers have also  
29  
30 investigated the material design and/or structural forms of the system [17-19]. For  
31  
32 instance, origami crush boxes and nested systems have been proposed because they  
33  
34 can improve the energy absorption efficiency and capacity, respectively [17-18].  
35  
36 Composite structures, such as sandwich beams and foam-filled tubes, have been used  
37  
38 in the energy-absorbing tube systems because they are lightweight and exhibit high  
39  
40 structural performance [20-23].  
41  
42  
43  
44  
45  
46  
47  
48

49  
50 Modifiability is an indispensable requirement associated with the  
51  
52 energy-absorbing devices because it is vital to respond quickly to ensure protection  
53  
54 under emergency circumstances. However, the conventional round-tube systems  
55  
56  
57

1  
2  
3  
4 require additional labor and time during installation with respect to the positioning of  
5  
6 structures and establishment of boundary constraints; thus, they are incapable of  
7  
8 modifiability or providing a quick response. Therefore, Chen et al. proposed a novel  
9  
10 self-locked energy-absorbing system in which tubes can interlock with each other and  
11  
12 no constraints are needed on the boundary or between the tubes [24, 25]. They also  
13  
14 proved that the ellipse-shaped self-locked tube is an optimal design when compared  
15  
16 with other conventional self-locked tubes [26]. The ellipse-shaped self-locked tube  
17  
18 not only overcomes the splashing of the tubes, as shown in Fig. 1, but also  
19  
20 significantly improves the energy absorption properties because it exhibits an  
21  
22 improved collapse stroke as well as energy dissipation potential per unit mass or  
23  
24 volume upon lateral compression, resulting in excellent energy absorption efficiency  
25  
26 [11, 26]. However, the ellipse-shaped self-locked tubes have never been theoretically  
27  
28 studied. The theoretical model can provide a fundamental understanding of the tube  
29  
30 response mechanics under loadings and investigate the effects of the geometric design  
31  
32 parameters on the energy absorption performance. Therefore, there have been  
33  
34 continuous demands to theoretically analyze the ellipse-shaped self-locked tubes.  
35  
36  
37  
38  
39  
40  
41  
42 Many researchers have studied the plastic deformation of the thin-walled round tubes  
43  
44 based on the plastic hinge theory, where plastic deformation is assumed to occur only  
45  
46 at the plastic hinges and the elastic deformation is neglected. Deruntz and Hodge  
47  
48 proposed a four-hinge mechanism to study the quasi-static lateral compression of a  
49  
50 circular tube between two parallel rigid plates [27]. Their model can approximately  
51  
52 predict the force–displacement curve; however, it neglects tube flattening. Burton and  
53  
54  
55  
56  
57  
58

Craig developed a six-hinge model to address the tube flattening problem [28]. Furthermore, Reid and Reddy proposed a hinge line theory, where the localized hinges were replaced by an arc exhibiting an adjustable length upon compression, and demonstrated its strong agreement with the experimental results [29].

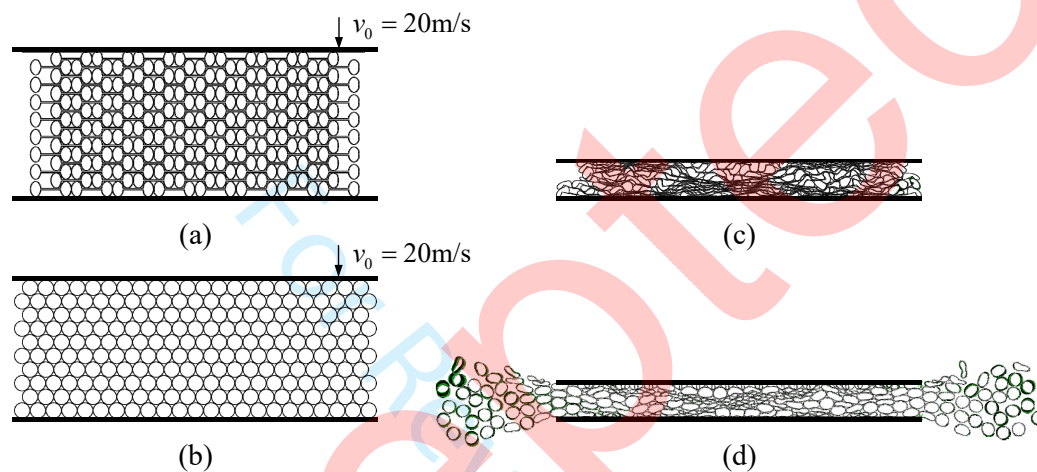


**Fig. 1.** Energy absorption systems under lateral impact: (a) ellipse-shaped self-locked system, and (b) conventional round tube system, and their deformed configurations (c)-(d) at 70% normalized displacement [26].

Here, we intend to establish a theoretical model for studying the force response of the ellipse-shaped self-locked tube under static compression, enabling the optimization of the design of the ellipse-shaped self-locked tube systems. Section 2 involves quasi-static experiments and finite element method (FEM) simulations of the tube for investigating the tube deformation under compression. Based on the experimental and simulation results, a plastic hinge model of the tube is established and presented in Section 3. Using the theoretical model, the effects of tuning the geometric parameters of the tube on the energy absorption performance are studied

and a guideline with respect to the design of the ellipse-shaped self-locked tubes is presented in Section 4. This work theoretically analyzes the force response and energy absorption performance of the ellipse-shaped self-locked tube and provides information about the structural design of the energy-absorbing systems in engineering applications, including aircraft, vessels, and automobiles.

## 2. Mechanical response of ellipse-shaped self-locked tube

To establish a theoretical model for the ellipse-shaped self-locked tube, quasi-static experiments and FEM simulations are firstly carried out in this section to investigate the mechanical response of the tube under compressive loadings.

### 2.1 Geometry of the ellipse-shaped self-locked tube

An ellipse-shaped self-locked tube is comprised of two open elliptical shells and two parallel flat plates, and the geometry is determined by 6 parameters as shown in Fig. 2(a) and (b): the length  $L$ , the width of flat plates  $W$ , the spacing between flat plates  $S$ , the thickness  $T$ , the horizontal semi-axis  $a$  and the vertical semi-axis  $b$ . In this paper, the shape of the tube is characterized by normalized geometry parameters, i.e. the normalized flat plate width  $\bar{W} = W/b$ , the normalized flat plate spacing  $\bar{S} = S/b$ , the normalized thickness  $\bar{T} = T/b$  and the ovality of the ellipse  $e = b/a$ .

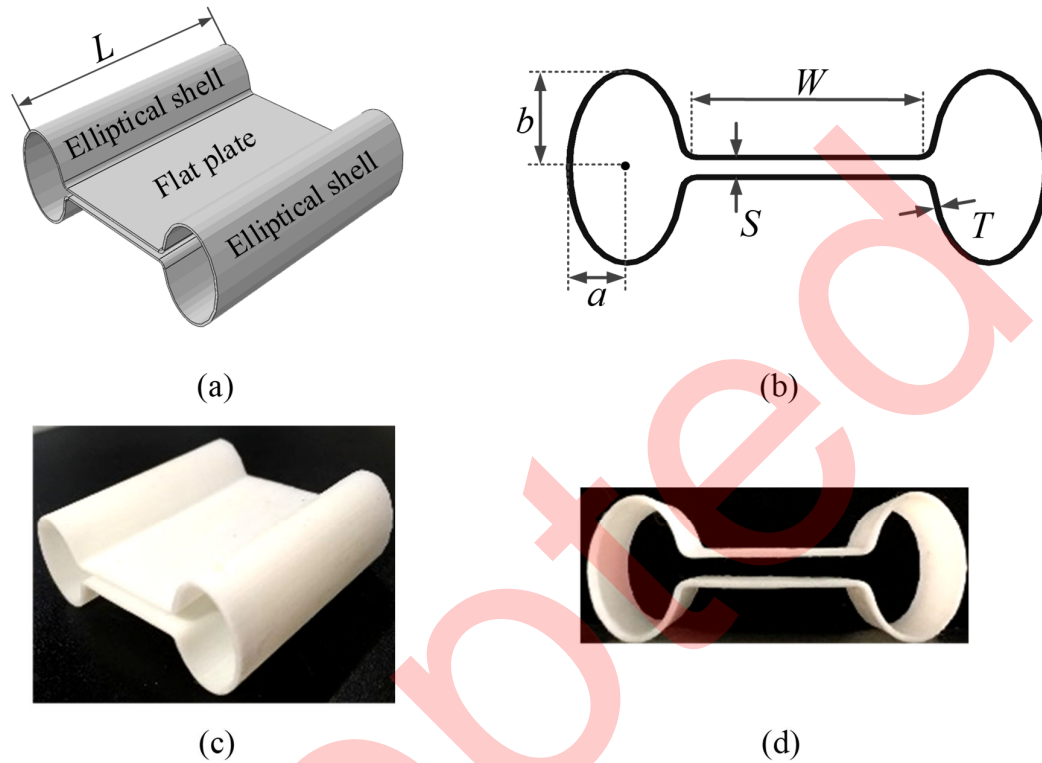


**Fig. 2.** Model of an ellipse-shaped self-locked tube from (a) isometric view and (b) side view, and experimental specimen from (c) isometric view and (d) side view.

## 2.2 Experimental specimen and setups

The ellipse-shaped self-locked tube specimen is manufactured by 3D printing using white photopolymer resin, as shown in Fig. 2(c) and (d). The mechanical properties of the material of experimental specimens are listed in Table 1, which are obtained from the tensile tests of the specimen material, with details provided in Appendix A1. The geometric parameters of specimens are provided in Table 2, and the chamfers with radius of 2mm are designed between the open elliptical shells and parallel flat plates.

**Table 1.** Material properties of white photopolymer resin.

Young's modulus (MPa)	Poisson ratio	Initial yield stress (MPa)	Hardening modulus (MPa)	Density (kg/m <sup>3</sup> )
225	0.4	22.5	7.5	1000

**Table 2.** Geometric parameters for tube specimen (mm).

Specimen	$L$	$W$	$S$	$T$	$a$	$b$
#1	49.8	31.5	2.8	1.0	7.4	9.7
#2	49.6	31.4	2.9	1.0	7.5	9.8
#3	49.7	41.7	3.0	1.0	9.9	10
#4	49.9	41.5	2.9	1.0	9.9	9.8

The quasi-static crushing experiments of the specimens #1 and #2 are conducted by Instron 5565-5kN test machine. The tube is placed between two rigid plates, as shown in Fig. 4(a)-(e). The lower supporting plate is fixed, and the crushing load is applied to the upper loading plate. The crushing loading speed is 0.5mm/min, which is sufficiently slow to suppress the dynamic effects, therefore this loading can be considered to be quasi-static. The measuring range of the load cell is up to 5kN, with accuracy of 0.5%. The load and the corresponding displacement are recorded per 0.1s.

### 2.3 Finite element simulation

The FEM simulation of the static compression of the ellipse-shaped self-locked tube model is conducted by ABAQUS/Standard, with geometric parameters same as the average of experimental specimens #1 and #2. The chamfers with radius of 2 mm are also designed between the open elliptical shells and parallel flat plates. The tube material is white photopolymer resin, and a bilinear elastic-plastic constitutive model

is employed in the simulation, with mechanical properties listed in Table 1. Because the length of the unit cell  $L$  is large enough, it satisfies the plane strain condition and the plane strain elements CPE4R are used in ABAQUS, with using 6 elements through thickness. In the simulation, the ellipse-shaped self-locked tube is constrained by the loading plate and the supporting plate. The two plates are both idealized as rigid bodies, and all degrees of freedom of the supporting plate are constrained. A vertical static displacement load is applied to the loading plate to crush the tube. The contact properties between surfaces are set as “surface to surface” and “hard” contact, and the friction coefficient is 0.05 [18, 25]. According to the tube configuration, loading symmetry as well as the deformed configurations observed in experiments as shown in Fig. 4(a)-(e), the tube is assumed to be doubly symmetric during the compressive process. Therefore, only a quarter model of the proposed tube is established in FEM simulation, and the symmetry boundary conditions are applied on the vertical and horizontal symmetry planes, respectively, as shown in Fig. 4(f)-(j).

## 2.4 Results and discussion

The force-displacement curves of the ellipse-shaped self-locked tube obtained from experiments and FEM simulation are depicted as blue curves with different markers and blue dashed curve in Fig. 3, respectively, and the deformed progress is presented in Fig. 4. The experimental and simulation results coincide well with each other, which validates the accuracy of the simulation model.

In Fig. 3, the displacement of the loading plate  $2\delta$  is normalized by the vertical axis length  $2b$  as  $\bar{\delta} = \delta/b$ . As shown in Fig. 3, the deformation of the tube can be

1  
2  
3  
4 divided into three phases. The force of the tube increases almost linearly with the  
5  
6 displacement at the beginning of phase I, because the mechanical behavior at this  
7  
8 moment is dominated by the elastic deformation. As the crushing progresses, some  
9  
10 part of the tube gradually goes into plastic stage. At about 10.6% normalized  
11  
12 displacement, the two flat plates of the tube contact each other, and the deformation of  
13  
14 the tube enters phase II. Due to the manufacture error, the specimens could enter  
15  
16 phase II earlier than the tube model in FEM simulation, as shown in Fig. 4(b) and (g).  
17  
18 As the crushing progresses, the upper and lower flat plates of the tube bend toward the  
19  
20 loading plate and the supporting plate, respectively, and the ellipses deform  
21  
22 significantly, as shown in Fig. 4(c) and (h). Phase II is the most important energy  
23  
24 absorption phase, because most crushing energy is absorbed in this process. With the  
25  
26 gradual increase of the compressive loading, the flat plates of the tube contact the  
27  
28 loading plate and the supporting plate, respectively, as shown in Fig. 4(d) and (i).  
29  
30 When the deformation of the tube enters phase III, as shown in Fig. 3, the force of the  
31  
32 tube increases sharply in this phase, and the tube is no longer suitable for energy  
33  
34 absorption.  
35  
36  
37  
38  
39  
40  
41  
42  
43  
44  
45  
46  
47  
48  
49  
50  
51  
52  
53  
54  
55  
56  
57  
58

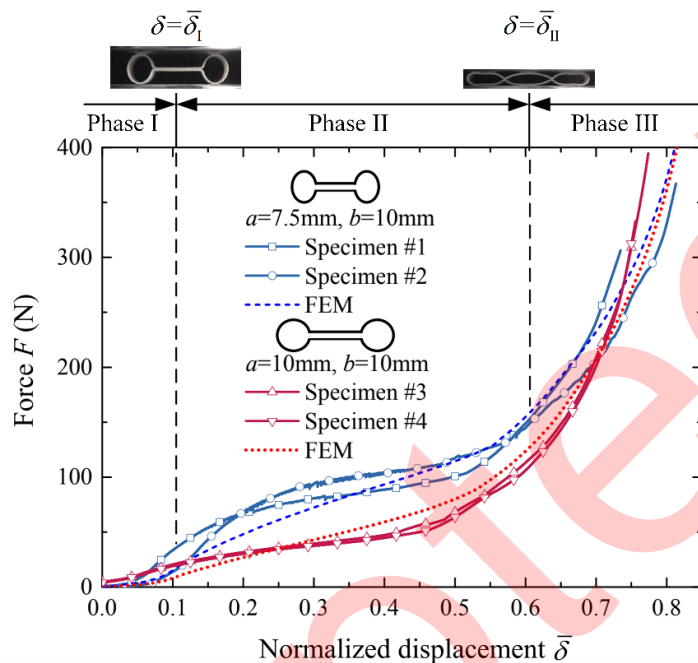


**Fig. 3.** The force-displacement curves of the ellipse-shaped self-locked tube model made of white photopolymer resin.

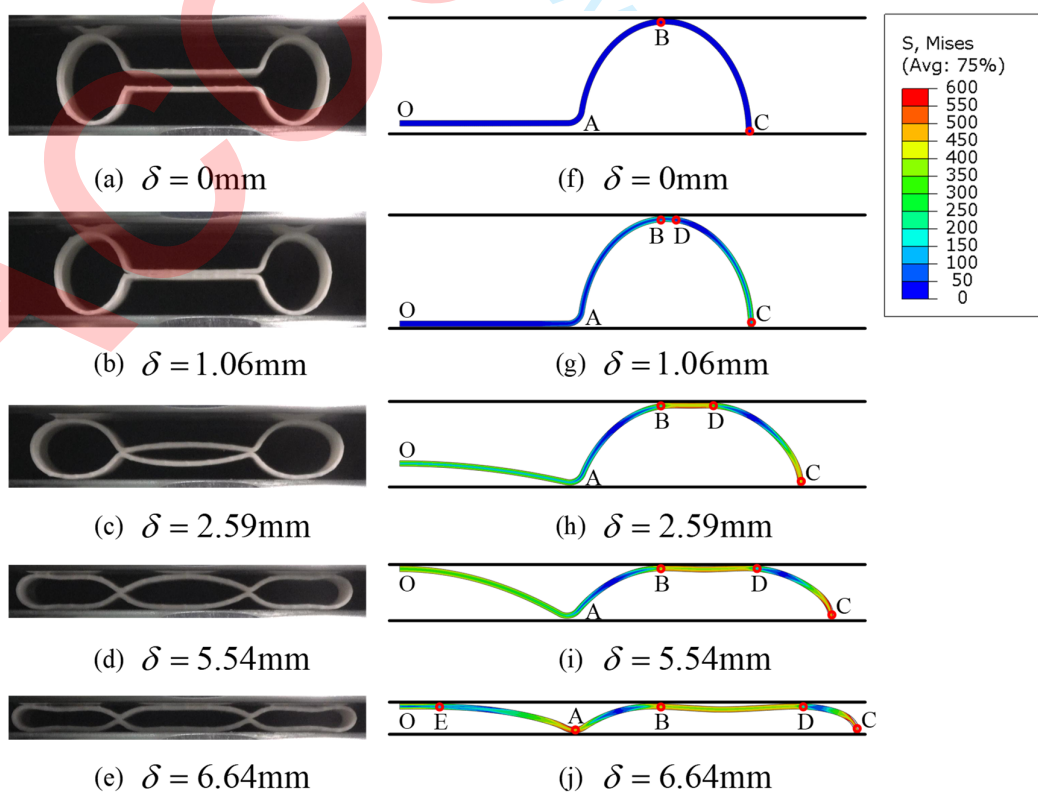


**Fig. 4.** Deformed configurations of the ellipse-shaped self-locked tube model with  $a=7.5\text{mm}$  and  $b=10\text{mm}$ : (a)-(e) quasi-static experiment and (f)-(j) FEM simulation.

As a comparison, the compression behavior of the previously proposed circle-shaped self-locked tube [24] is also studied by quasi-static experiment and FEM simulation. The geometric parameters of circle-shaped self-locked tube specimens #3 and #4 are provided in Table 2, and the results are depicted as red lines with different markers and red dashed line in Fig. 3, respectively. Compared with the circle-shaped self-locked tube, the ellipse-shaped self-locked tube improves the energy absorption capacity significantly.

### 3 Theoretical model of the ellipse-shaped self-locked tubes

Based on above experimental and simulation results, the crushing process of the tube is firstly dominated by elastic deformation in a very short region, and then goes into plastic deformation dominated region soon. To analyze the energy absorption performance of the tube theoretically, the elastic deformation is ignored and a plastic hinge model of the tube is established in this section.

#### 3.1 Plastic hinge model

According to the deformed configurations observed in Fig. 4, a plastic hinge model is developed herein with the following assumptions [27, 30].

- (1) The elastic deformation is ignored.
- (2) The plastic deformation only occurs at the plastic hinges.
- (3) The plastic hinge is approximated as a region of length  $\lambda=4T$ , which is

much smaller compared with the tube size, and thus undergoes uniform change in curvature  $\Delta k$  [29].

(4) The friction is neglected.

In engineering fields, the energy absorption structures are mostly made of metal to improve the energy absorption capacity. Therefore, the rigid-plastic model with isotropic linear hardening is adopted here to describe the constitutive relation of material

$$\sigma_m(\varepsilon_m) = \sigma_s + E_p \varepsilon_m \quad (1)$$

where  $\sigma_m$ ,  $\varepsilon_m$ ,  $E_p$  and  $\sigma_s$  are the stress, strain, plastic hardening modulus and uniaxial yield stress of tube material, respectively. The moment  $M$  at plastic hinges is expressed as [18, 27]

$$M = M_0 \left( 1 + \frac{E_p T}{3\sigma_s} \cdot \Delta k \right) \quad (2)$$

where  $M_0 = \sigma_s T^2 L / 4$  is the yield moment,  $T$  is the tube thickness and  $\Delta k$  is the change of curvature. Similar with the FEM simulation model, only a quarter of the ellipse-shaped self-locked tube is considered in developing the plastic hinge model.

According to the discussion in Section 2, the deformation of the ellipse-shaped self-locked tube model presents a three-phase behavior. Fig. 4(f) illustrates the initial configuration of the model, and the plastic deformation initiates at points B and C. In phase I, a deformation zone  $\widehat{BD}$  is generated and attached to the loading plate because the plastic hinge D originates from point B and travels along the elliptical arc  $\widehat{BC}$ . Arc  $\widehat{OAB}$  is assumed to be rigid and move downwards in this phase. As the crushing progresses, the flat plates of the tube contact each other, and the deformation

of the tube enters phase II, as shown in Fig. 4(g). The deformation zone  $\widehat{BD}$  is enlarged significantly, and the deformed configuration of arc  $\widehat{DC}$  is the same as that of phase I. The flat plate  $\widehat{OA}$  of the tube begins to bend towards the loading plate, as shown in Fig. 4(h). However, the angle between arc  $\widehat{OA}$  and arc  $\widehat{AB}$  keeps constant. When the upper flat plate touches the loading plate as shown in Fig. 4(i), the deformation of the tube enters phase III. In phase III, the angle between arc  $\widehat{OA}$  and arc  $\widehat{AB}$  is enlarged, and a deformation zone  $\widehat{OE}$  is generated and attached to the loading plate because the plastic hinge E originates from point O and travels along the elliptical arc  $\widehat{OA}$ . In this paper, the force on the tube is divided into two parts, one is the force  $F_B$  on arc  $\widehat{OAB}$  in phases I, II and III, and the other is the force  $F_D$  on arc  $\widehat{CD}$ .

### 3.2 Force analysis of arc $\widehat{OAB}$

#### (1) Phase I

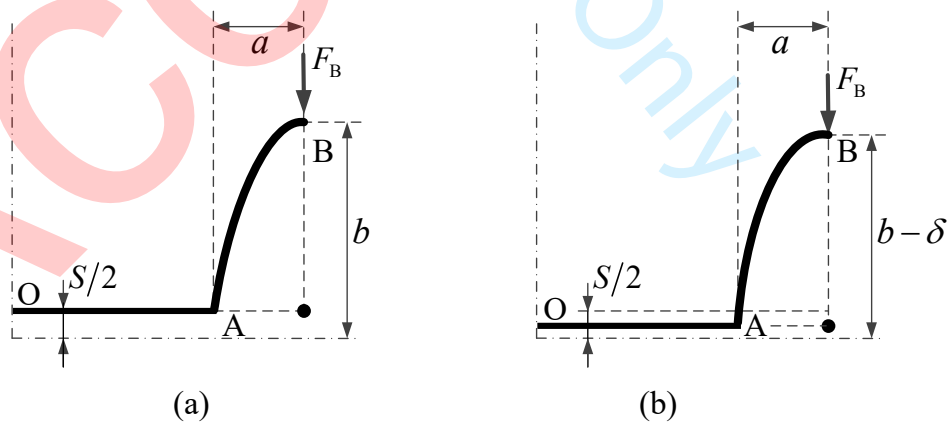


**Fig. 5.** Plastic hinge model of arc  $\widehat{OAB}$  in phase I: (a) initial configuration and (b) deformed configuration.

In phase I, arc  $\widehat{OAB}$  is assumed as a rigid body moving downwards until the

flat plate  $\widehat{OA}$  reaching the horizontal symmetry plane, as shown in Fig. 5. Therefore, arc  $\widehat{OAB}$  has no plastic deformation, and the crushing force at point B in phase I can be expressed as

$$F_B = 0, \quad (0 \leq \bar{\delta} < \bar{\delta}_1) \quad (3)$$

where  $\bar{\delta}_1$  is the normalized displacement of the loading plate at the end of phase I and equals

$$\bar{\delta}_1 = \frac{\bar{S}}{2} \quad (4)$$

(2) Phase II

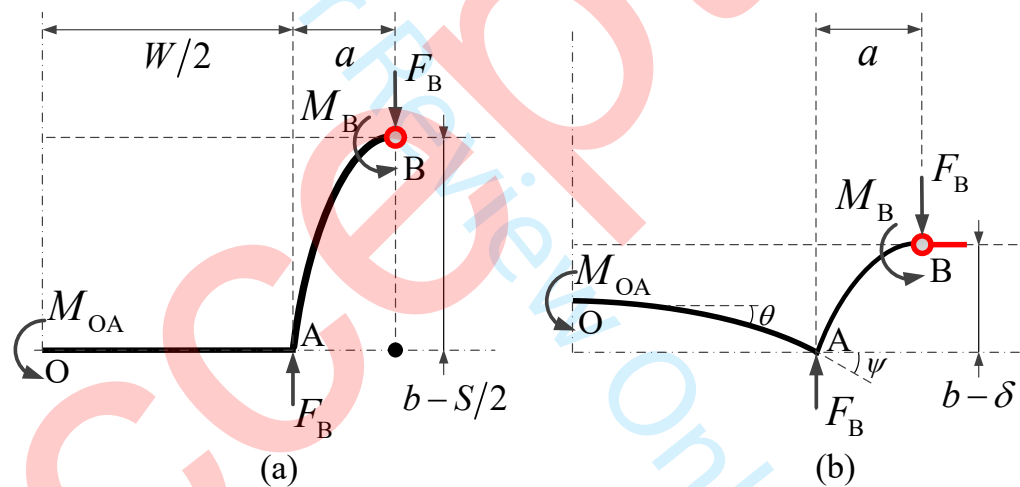


**Fig. 6.** Plastic hinge model of arc  $\widehat{OAB}$  in phase II: (a) hinge formation and (b) deformed configuration.

The flat plate  $\widehat{OA}$  starts to bend due to the bending moment  $M_{OA}$  in phase II, and the curvature change of the plate  $\widehat{OA}$  is uniformly distributed because the friction at point A is neglected, as shown in Fig. 6. Based on the assumption (2) of plastic hinge, arc  $\widehat{OA}$  is idealized as a plastic hinge of length  $\lambda_{OA} = W/2$  in this phase. In phase II, a plastic hinge is generated at point B, and the horizontal

displacement between hinge B and point A is assumed to remain as a constant length  $a$  during the whole compressive process, which had been shown by the experimental and simulation deformation depicted in Fig. 4(c)-(e) and (h)-(j). Moreover, the elliptical arc  $\widehat{AB}$  is assumed as a rigid body connected by two plastic hinges  $\widehat{OA}$  and B, and it rotates clockwise. The angle between arc  $\widehat{AB}$  and arc  $\widehat{OA}$  at point A is considered to be constant.

The equilibrium of moment of arc  $\widehat{AB}$  with respect to point A is

$$F_B \cdot a = M_{OA} + M_B \quad (5)$$

where  $F_B$  is the force at hinge B, and  $M_{OA}$  and  $M_B$  are the moments at hinges  $\widehat{OA}$  and B, respectively. According to the assumptions above, arc  $\widehat{AB}$  can be assumed as a quarter of an ellipse tube with horizontal semi-axis  $a$  and vertical semi-axis  $b - \delta$ , as shown in Fig. 6(b). Based on the curvature equation of the ellipse, the curvature change at point B is  $\Delta k_B = (b - \delta)/a^2$ . According to Eq. (2), the moment at point B is

$$M_B = M_0 \left( 1 + \frac{E_p T}{3\sigma_s} \cdot \frac{b - \delta}{a^2} \right) \quad (6)$$

For elliptical arc  $\widehat{ABC}$ , because the flat plates spacing  $S$  is much smaller than initial horizontal semi-axis  $a$  and vertical semi-axis  $b$ , we assume that the inclined angles of arc  $\widehat{AB}$  at point A and  $\widehat{DC}$  at point C equal and denote them as  $\psi$ , as shown in Fig. 6. The inclined angle of arc  $\widehat{OA}$  at point O is zero, therefore the inclined angle of arc  $\widehat{OA}$  is  $\psi$  and the deformed curvature of arc  $\widehat{OA}$  is

$$\Delta k_{OA} = \frac{2\psi}{W} \quad (7)$$

According to Eqs. (2) and (7), the moment  $M_{OA}$  can be expressed as

$$M_{OA} = M_0 \left( 1 + \frac{E_p T}{3\sigma_s} \cdot \frac{2\psi}{W} \right) \quad (8)$$

Substituting Eqs. (6) and (8) into Eq. (5), the crushing force at point B in phase II is expressed as

$$F_B = \frac{\sigma_s \bar{T}^2 L e^2 a}{2} + \frac{E_p \bar{T}^3 L e^3 a}{12} \left[ e(1 - \bar{\delta}) + \frac{2\psi}{\bar{W}e} \right], \quad (\bar{\delta}_I \leq \bar{\delta} < \bar{\delta}_{II}) \quad (9)$$

where  $\bar{\delta}_{II}$  is the normalized displacement of the loading plate at the end of phase II.

According to the deformed configuration in Fig. 7(a),  $\bar{\delta}_{II}$  satisfies

$$\frac{\bar{W}}{2\psi_{II}} \cdot (1 - \cos\psi_{II}) = 1 - \bar{\delta}_{II} \quad (10)$$

where  $\psi_{II}$  is the inclined angle of arc  $\widehat{OA}$  at the end of phase II. The normalized displacement  $\bar{\delta}$  is the function of  $\psi$ , with the detailed expression provided in Section 3.3, therefore the inclined angle  $\psi_{II}$  and the normalized displacement  $\bar{\delta}_{II}$  can be obtained from Eq. (10).

### (3) Phase III

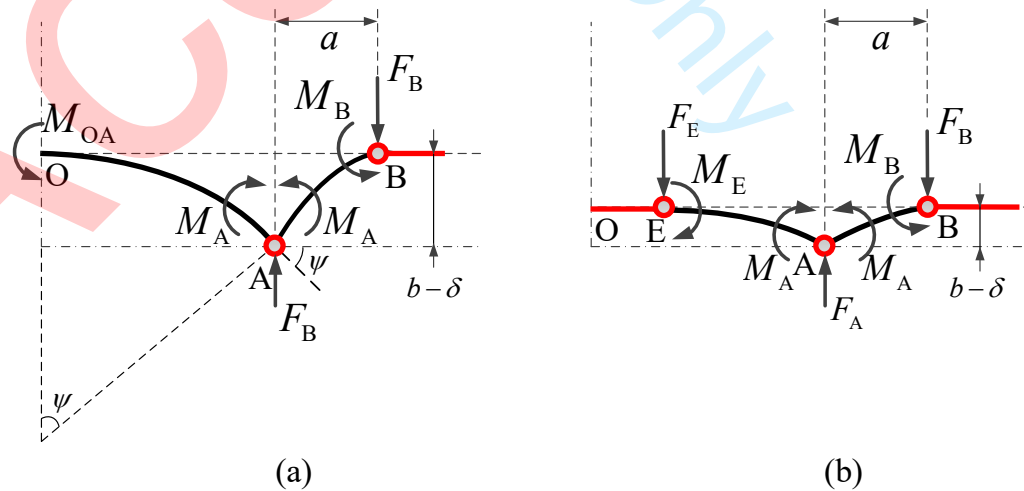


**Fig. 7.** Plastic hinge model of arc  $\widehat{OAB}$  in phase III: (a) hinge formation and (b) deformed configuration.

In phase III, the circular plate  $\widehat{OA}$  is also compressed and gradually attached to the loading plate as shown in Fig. 7, and two plastic hinges are generated at points A and E. The plastic hinge at point A is assumed as a fixed hinge, and the plastic hinge at point E is a travelling hinge moving from point O to point A so that arc  $\widehat{OA}$  can be fully attached to the loading plate, as shown in Fig. 7(b). The circular arc  $\widehat{EA}$  is treated as a rigid body and rotates anti-clockwise. The angle between arc  $\widehat{AB}$  and  $\widehat{OA}$  at point A is increased in this phase, therefore the bending moment  $M_A$  is occurring at point A. In phases I and II, the total crushing force of  $\widehat{OAB}$   $F_{\widehat{OAB}}$  equals  $F_B$ . Because a new plastic hinge is formed as point E in phase III, the force  $F_{\widehat{OAB}}$  of phase III satisfies

$$F_{\widehat{OAB}} = F_B + F_E \quad (11)$$

where  $F_B$  and  $F_E$  can be obtained from the equilibrium of moment of the curved arcs  $\widehat{EA}$  and  $\widehat{AB}$ , respectively, as

$$F_E \cdot \sqrt{\left(\frac{W}{2\psi}\right)^2 - \left(\frac{W}{2\psi} - b + \delta\right)^2} = M_E + M_A \quad (12)$$

and

$$F_B \cdot a = M_B + M_A \quad (13)$$

where the expression of  $M_B$  can be found in Eq. (6). According to isotropic hardening assumption, the moment of arc  $\widehat{EA}$  is

$$M = M_0 \cdot \left[ 1 + \frac{E_p T}{3\sigma_s} \cdot (\Delta k_{EA} + \Delta k') \right] \quad (14)$$

where  $\Delta k_{EA}$  is the deformed curvature of the arc  $\widehat{EA}$  at the beginning of phase III,

and  $\Delta k'$  is the additional curvature change of  $\widehat{EA}$  in phase III. Therefore, the moments at hinges E and A can be expressed as

$$M_E = M_0 \cdot \left[ 1 + \frac{E_p T}{3\sigma_s} \cdot (\Delta k_{EA} + \Delta k'_E) \right] \quad (15)$$

and

$$M_A = M_0 \cdot \left[ 1 + \frac{E_p T}{3\sigma_s} \cdot (\Delta k_{EA} + \Delta k'_A) \right] \quad (16)$$

The deformed curvature of the arc  $\widehat{EA}$  at the beginning of phase III is the same with that of  $\widehat{OA}$  at the end of phase II and is obtained from

$$\Delta k_{EA} = \frac{2\psi_{II}}{W} \quad (17)$$

The additional curvature changes at hinges E and A in phase III are

$$\Delta k'_E = \frac{2\psi_{II}}{W} \quad (18)$$

and

$$\Delta k'_A = \frac{1}{\lambda_A} \cdot \left[ (\psi - \psi_{II}) + \left( \arccos \frac{\frac{W}{2\psi_{II}} - b + \delta_{II}}{\frac{W}{2\psi_{II}}} - \arccos \frac{\frac{W}{2\psi} - b + \delta}{\frac{W}{2\psi}} \right) \right] \quad (19)$$

where  $\lambda_A$  is the effective hinge length of point A, which is assumed to be four times of the wall thickness, i.e.  $\lambda_A = 4T$  [18, 25, 30].

Based on the above equations, the force  $F_{\widehat{OAB}}$  of phase III can be expressed as

$$\begin{aligned}
 F_{\widehat{OAB}} = & \frac{\sigma_s \bar{T}^2 L e^2 a}{2} + \frac{E_p \bar{T}^3 L e^2 a}{12} \cdot \left[ e^2 (1 - \bar{\delta}) + \frac{2\psi_{II}}{\bar{W}} \right. \\
 & \left. + \frac{\psi - \psi_{II} + \arccos \frac{\bar{W} - 2\psi_{II}(1 - \bar{\delta}_{II})}{\bar{W}} - \arccos \frac{\bar{W} - 2\psi(1 - \bar{\delta})}{\bar{W}}}{4\bar{T}} \right] \\
 & + \frac{1}{12 \sqrt{\frac{\bar{W}}{\psi} (1 - \bar{\delta}) - (1 - \bar{\delta})^2}} \cdot \left[ 6\sigma_s \bar{T}^2 L e a + E_p \bar{T}^3 L e a \right. \\
 & \left. \cdot \left( \frac{6\psi_{II}}{\bar{W}} + \frac{\psi - \psi_{II} + \arccos \frac{\bar{W} - 2\psi_{II}(1 - \bar{\delta}_{II})}{\bar{W}} - \arccos \frac{\bar{W} - 2\psi(1 - \bar{\delta})}{\bar{W}}}{4\bar{T}} \right) \right] \\
 & (\bar{\delta}_{II} \leq \bar{\delta} < 1) \quad (20)
 \end{aligned}$$

From the results in Fig. 4, the additional curvature change at hinge A  $\Delta k'_A$  in Phase III is limited. Thus Eq. (20) can be simplified as

$$\begin{aligned}
 F_{\widehat{OAB}} = & \frac{\sigma_s \bar{T}^2 L e^2 a}{2} + \frac{E_p \bar{T}^3 L e^2 a}{12} \cdot \left[ e^2 (1 - \bar{\delta}) + \frac{2\psi_{II}}{\bar{W}} \right] + \\
 & + \frac{1}{12 \sqrt{\frac{\bar{W}}{\psi} (1 - \bar{\delta}) - (1 - \bar{\delta})^2}} \cdot \left( 6\sigma_s \bar{T}^2 L e a + E_p \bar{T}^3 L e a \cdot \frac{6\psi_{II}}{\bar{W}} \right) \quad (21)
 \end{aligned}$$

### 3.3 Force analysis of arc $\widehat{CD}$

When conducting force analysis of arc  $\widehat{CD}$ , we assume that the plastic zone originates from point C and extends towards point D, because the largest bending moment of arc  $\widehat{CD}$   $M_c$  occurs at point C. Point D is assumed as a hinge moving rightwards, and arc  $\widehat{CF}$  is assumed as a hinge whose length is increasingly enlarged during the compression process, as shown in Fig. 8(a) and (b). The ellipse arc  $\widehat{DF}$  is assumed as a rigid body connected by these two hinges, and rotates anti-clockwise with angle  $\psi$  from its original position, as shown in Fig. 8(a).

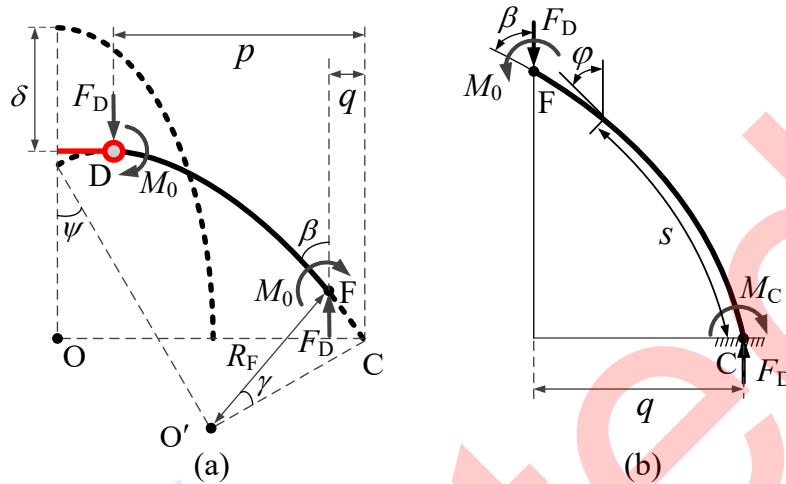


Fig. 8. Plastic hinge model of (a) arc  $\widehat{DF}$  and (b) arc  $\widehat{FC}$ .

Based on approximately differential equation of the deflection curve, it can be obtained from Fig. 8(b) that [11, 12]

$$E_p I \frac{d^2 \varphi}{ds^2} = -F_D \sin \varphi \quad (22)$$

where  $F_D$  is the force at hinge D,  $I = T^3 L / 12$  is the second moment of the cross section,  $\varphi$  is the curved beam angle and  $s$  is the curved beam length. Eq. (22) can be integrated as

$$\frac{E_p I}{2} \left( \frac{d\varphi}{ds} \right)^2 = F_D \cos \varphi + C \quad (23)$$

where  $C$  is an arbitrary constant. The curved beam angle at point E satisfies  $\varphi = \beta$ ,

therefore the curvature of arc  $\widehat{FC}$  at point E can be expressed as

$$\left( \frac{d\varphi}{ds} \right)_{\varphi=\beta} = \frac{1}{R_F} = \frac{e}{a} \left( \sin^2 \gamma + e^2 \cos^2 \gamma \right)^{-\frac{3}{2}} \quad (24)$$

where  $R_F$  is the radius of curvature of arc  $\widehat{FC}$  at point E and  $\gamma$  is the angle between segments  $O'C$  and  $OF$  which satisfies  $\gamma = \beta - \psi$ . Substituting Eq. (24) into Eq. (23),

we obtain that

$$\left(\frac{d\varphi}{ds}\right)^2 = \frac{2F_D}{E_p I} (\cos\varphi - \cos\beta) + \frac{1}{R_F^2} \quad (25)$$

As shown in Fig. 8(b), the equilibrium of moment of arc  $\widehat{FC}$  with respect to C is

$$M_C = M_0 + F_D q \quad (26)$$

where  $q$  is the horizontal displacement between points F and C. The bending moment  $M_C$  of arc  $\widehat{FC}$  at point C can also be expressed as

$$M_C = M_0 + E_p I \left[ \left(\frac{d\varphi}{ds}\right)_{\varphi=0} - \frac{1}{a} \right] \quad (27)$$

From Eqs. (26) and (27), we obtain that

$$\left(\frac{d\varphi}{ds}\right)_{\varphi=0} = \frac{F_D q}{E_p I} + \frac{1}{a} \quad (28)$$

Substituting Eq. (28) into Eq. (25), we obtain that

$$\frac{F_D^2}{E_p^2 I^2} q^2 + \frac{2F_D}{E_p I a} q - \frac{2F_D}{E_p I} (1 - \cos\beta) + \frac{1}{a^2} - \frac{1}{R_F^2} = 0 \quad (29)$$

As shown in Fig. 8(a), the equilibrium of moment of arc  $\widehat{DF}$  with respect to F is

$$F_D \cdot (p - q) = 2M_0 \quad (30)$$

where  $p$  is the horizontal displacement between points D and C, and can be calculated by

$$p(\psi) = a \cos\psi + a(e^2 - 1) \sin\psi \cos\psi \sqrt{\frac{e^2 \sin^2\psi + \cos^2\psi}{(e^2 - 1)^2 \sin^2\psi \cos^2\psi + e^2}} \quad (31)$$

The detailed analysis of  $p(\psi)$  can be found in Appendix A2.

Substituting Eq. (30) into Eq. (29), we obtain the positive root of the force at hinge D  $F_D$  as follows

$$F_D = \frac{2M_0pa - E_p I (p + a \cos \beta - a)}{p^2 a} + \frac{1}{p^2 a} \cdot \sqrt{\left[ E_p I (p + a \cos \beta - a) - 2M_0pa \right]^2 - E_p I p^2 \left( \frac{4M_0^2 a^2}{E_p I} - 4M_0a + E_p I - \frac{E_p I a^2}{R_F^2} \right)} \quad (0 \leq \bar{\delta} < 1) \quad (32)$$

where the expressions of  $M_0$ ,  $R_F$ ,  $p$  and  $I$  can be found in above analysis. Denoting that

$\beta = k\psi$ , we obtain that

$$\gamma = \beta - \psi = (k - 1)\psi \quad (33)$$

Based on previous work [11], we assume that  $k = 1.6$  in this paper.

The normalized vertical displacement of the loading plate  $\bar{\delta}$  can be expressed as

$$\bar{\delta}(\psi) = 1 + \frac{\sin \psi}{e} - \frac{1}{e} \sqrt{\frac{(e^2 - 1)^2 \sin^2 \psi \cos^2 \psi + e^2}{e^2 \sin^2 \psi + \cos^2 \psi}} \quad (34)$$

The detailed analysis of  $\bar{\delta}(\psi)$  can be found in Appendix A2.

### 3.4 Constitutive relation of ellipse-shaped self-locked tube

Because of symmetry, the crushing force  $F$  of an ellipse-shaped self-locked tube can be obtained by  $F_{\text{total}} = 2(F_{\text{OAB}} + F_D)$ , therefore we obtain that

$$\begin{aligned}
F_{\text{total}}(\psi) = & \\
& \left[ \frac{E_p \bar{T}^2 L e^2 a^2}{6p(\psi)} \cdot \left\{ \frac{6\sigma_s}{E_p} - \bar{T}e \left[ 1 + \frac{a \cos(k\psi) - a}{p(\psi)} \right] \right. \right. \\
& + \sqrt{\left. \left. \left[ \frac{6\sigma_s}{E_p} - \bar{T}e \left( 1 + \frac{a \cos(k\psi) - a}{p(\psi)} \right) \right]^2 - 12\bar{T}^2 e^2 \left[ \frac{3\sigma_s^2}{E_p^2 \bar{T}^2 e^2} - \frac{\sigma_s}{E_p \bar{T}e} + \frac{1}{12} - \frac{a^2}{12R_F^2(\psi)} \right]} \right\} \\
& \quad \quad \quad (0 \leq \bar{\delta}(\psi) < \bar{\delta}_I) \\
& \sigma_s \bar{T}^2 L e^2 a + \frac{E_p \bar{T}^3 L e^3 a}{6} \cdot \left[ e(1 - \bar{\delta}) + \frac{2\psi}{\bar{W}e} \right] \\
& + \frac{E_p \bar{T}^2 L e^2 a^2}{6p(\psi)} \cdot \left\{ \frac{6\sigma_s}{E_p} - \bar{T}e \left[ 1 + \frac{a \cos(k\psi) - a}{p(\psi)} \right] \right. \\
& + \sqrt{\left. \left. \left[ \frac{6\sigma_s}{E_p} - \bar{T}e \left( 1 + \frac{a \cos(k\psi) - a}{p(\psi)} \right) \right]^2 - 12\bar{T}^2 e^2 \left[ \frac{3\sigma_s^2}{E_p^2 \bar{T}^2 e^2} - \frac{\sigma_s}{E_p \bar{T}e} + \frac{1}{12} - \frac{a^2}{12R_F^2(\psi)} \right]} \right\} \\
& \quad \quad \quad (\bar{\delta}_I \leq \bar{\delta}(\psi) < \bar{\delta}_{II}) \\
& \sigma_s \bar{T}^2 L e^2 a + \frac{E_p \bar{T}^3 L e^2 a}{6} \cdot \left[ e^2(1 - \bar{\delta}) + \frac{2\psi_{II}}{\bar{W}} \right] \\
& + \frac{1}{6\sqrt{\frac{\bar{W}}{\psi}(1 - \bar{\delta}) - (1 - \bar{\delta})^2}} \cdot \left( 6\sigma_s \bar{T}^2 L e a + E_p \bar{T}^3 L e a \cdot \frac{6\psi_{II}}{\bar{W}} \right) \\
& + \frac{E_p \bar{T}^2 L e^2 a^2}{6p(\psi)} \cdot \left\{ \frac{6\sigma_s}{E_p} - \bar{T}e \left[ 1 + \frac{a \cos(k\psi) - a}{p(\psi)} \right] \right. \\
& + \sqrt{\left. \left. \left[ \frac{6\sigma_s}{E_p} - \bar{T}e \left( 1 + \frac{a \cos(k\psi) - a}{p(\psi)} \right) \right]^2 - 12\bar{T}^2 e^2 \left[ \frac{3\sigma_s^2}{E_p^2 \bar{T}^2 e^2} - \frac{\sigma_s}{E_p \bar{T}e} + \frac{1}{12} - \frac{a^2}{12R_F^2(\psi)} \right]} \right\} \\
& \quad \quad \quad (\bar{\delta}_{II} \leq \bar{\delta}(\psi) < 1)
\end{aligned} \tag{35}$$

where the expressions of  $R_F(\psi)$ ,  $p(\psi)$  and  $\bar{\delta}(\psi)$  can be found in Eqs. (24), (31)

and (34), respectively.

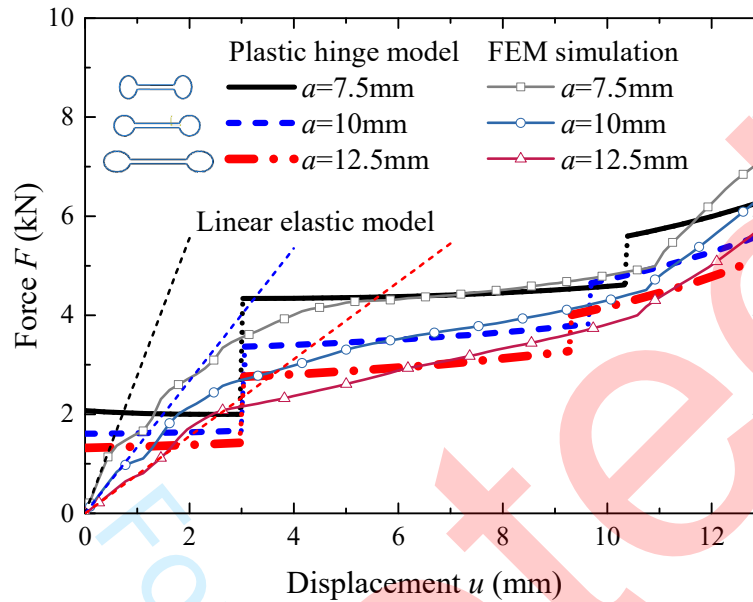


**Fig. 9.** The force-displacement curves of the ellipse-shaped self-locked tube model made of 201 stainless steel with vertical semi-axis  $b=10\text{mm}$ .

Based on Eq. (35), the force-displacement curves of the tubes made of 201 stainless steel obtained from the plastic hinge model are presented in Fig. 9. The mechanical properties of 201 stainless steel are listed in Table 3, and the geometric parameters are provided in Table 4. From the results, the tube with larger ovality  $e$  displays larger energy absorption capacity, and the critical displacement between phases II and III is also larger. The FEM simulation results of the tubes with the same geometric and mechanical parameters are also obtained and presented in Fig. 9 for the comparison purpose. At the beginning of the crushing, the FEM simulation forces increase with an approximate linear relationship with the displacement because the crushing in this phase is dominated by the elastic deformation. In elastic stage, the deformation of the tube can be predicted by the linear elastic analysis, with details in

Appendix A3 and results shown by dashed curves. Since the elastic deformation is neglected in the plastic hinge model, the forces predicted by the plastic hinge model remain almost constant. In phase II, the plastic deformation becomes dominant part, therefore the prediction of the plastic hinge model is getting close to the FEM simulation results. From discussions above, phase II is the most important energy absorption process, and the force of the tube in phase II is almost horizontal as shown in Fig. 9, indicating an excellent performance of energy absorption. In phase III, the prediction of plastic hinge model gradually goes lower than the results of FEM simulation. This underestimation of crushing forces at large crushing displacement is also observed in the theoretical models of round tube [27, 30]. This is because the effect of strain hardening and the reduction in hinge length are ignored in the theoretical model [29].

**Table 3.** Material properties of 201 stainless steel.

Young's modulus (GPa)	Poisson ratio	Initial yield stress (MPa)	Hardening modulus (MPa)	Density (kg/m <sup>3</sup> )
191	0.26	322	1100	7830

**Table 4.** Geometric parameters of the tubes (mm).

$L$	$W$	$S$	$T$	$a$	$b$
50	32	3	1	7.5	10
50	42	3	1	10	10
50	52	3	1	12.5	10

The relative error of the total energy absorption  $EA$  of the three tube models

between plastic hinge model and FEM simulation are provided in Table 5. Herein  $EA$  is defined as the total energy absorbed by the tube before densification, with detailed definition provided in Section 4.1. The tube is no longer suitable for energy absorption in phase III, thus only the results in phases I and II are compared. From the results, the theoretical and simulation results coincide well with each other, which proves that the proposed plastic hinge model is accurate and can be used into the following optimization.

**Table 5.** The relative error of the total energy absorption  $EA$  of the three tube models between plastic hinge model and FEM simulation ( $b=10\text{mm}$ ).

$a$ (mm)	Relative error (%)	
	Phase I	Phase II
7.5	5.74	2.82
10	4.93	1.61
12.5	12.6	3.55

#### 4. Optimization of the tube

Based on the plastic hinge model established in Section 3, the effects of the tube geometric parameters on energy absorption properties are investigated in this section, and a guideline for designing the ellipse-shaped tube is provided.

##### 4.1 The key performance indicators

For a well-designed energy absorption element, large energy absorption capacity, high efficiency and long effective stroke ratio are all in a great demand. To find an optimal solution, the total energy absorption  $EA$ , the mass specific energy absorption

1  
2  
3  
4  $SEAm$ , the volume specific energy absorption  $SEAv$ , the normalized energy absorption  
5  
6 efficiency  $\bar{\eta}$  and the effective stroke ratio  $ESR$  are adopted as basic energy  
7  
8 absorption performance indicators.  
9

10 Here the total energy absorption  $EA$  is calculated by

$$11 \quad EA = \int_0^{2\delta_{\max}} F du \quad (36)$$

12 where  $u$  is the displacement of the loading plate, and  $\delta_{\max}$  is the maximum half  
13  
14 displacement of the loading plate taken into consideration, taken as  $\delta_{\max} = \delta_{II}$  [8, 24,  
15  
16  
17  
18  
19  
20  
21  
22 31]

23 The mass specific energy absorption  $SEAm$  is defined as the energy absorption  
24  
25 per unit mass [22, 32]

$$26 \quad SEAm = \frac{EA}{m} \quad (37)$$

27 and the volume specific energy absorption  $SEAv$  is defined as [33]

$$28 \quad SEAv = \frac{EA}{V} \quad (38)$$

29 where  $m$  is the mass of the tube and given by

$$30 \quad m = 2\rho\bar{T}Lea^2 \left\{ \left[ 4 \max(e, 1) + (2\pi - 4) \cdot \min(e, 1) \right] \cdot \left[ 1 - \frac{\arctan\left(\frac{\bar{S}e}{2}\right)}{\pi} \right] + \bar{W}e \right\} \quad (39)$$

31 and  $V$  is the space volume taken by the tube, expressed as

$$32 \quad V = Lea^2 \left[ 2\pi + e\bar{W}(\bar{S} + \bar{T}) \right] \quad (40)$$

33 The normalized energy absorption efficiency  $\bar{\eta}$  is defined as the ratio of the  
34  
35 mean loads  $F_{\text{mean}} = EA/2\delta_{\max}$  to the maximum force  $F_{\max}$ , which can be expressed as  
36  
37  
38  
39  
40  
41  
42  
43  
44  
45  
46  
47  
48  
49  
50  
51  
52  
53  
54  
55  
56  
57  
58  
59  
60 [22, 32, 34]

$$\bar{\eta} = \frac{F_{\text{mean}}}{F_{\text{max}}} = \frac{\int_0^{2\delta_{\text{max}}} F du}{2\delta_{\text{max}} \cdot F_{\text{max}}} \quad (41)$$

Here  $F_{\text{max}}$  is defined as the maximum force during the compression process from  $\delta = 0$  to  $\delta = \delta_{\text{II}}$ . The normalized energy absorption efficiency  $\bar{\eta}$  can reach the maximum of 100% only when the reaction force  $F$  is constant.

The effective stroke ratio  $ESR$  is defined as the ratio of the effective stroke to the original height of the tube under compression. The concept of  $ESR$  is similar with the densification strain for cellular materials. In this study, phase III is the densification stage of the tube, therefore, the effective stroke is adopted as the total compressive displacement at the end of phase II, and the effective stroke ratio  $ESR$  is expressed as [22, 32]

$$ESR = \bar{\delta}_{\text{II}} \quad (42)$$

#### 4.2 Geometry effects on energy absorption properties

The geometry of tube cross-section is determined by the vertical semi-axis  $b$ , the ovality  $e$ , the normalized thickness  $\bar{T}$ , the normalized flat plate width  $\bar{W}$  and the normalized flat plate spacing  $\bar{S}$ . To investigate the effects of these parameters on the energy absorption performance indicators established above, a series of geometry data are substituted into the theoretical model proposed in Section 3. The data range of these geometric parameters are selected as  $4\text{mm} \leq b \leq 20\text{mm}$ ,  $0.5 \leq e \leq 2.5$ ,  $0.04 \leq \bar{T} \leq 0.2$ ,  $3 \leq \bar{W} \leq 5.4$  and  $0.15 \leq \bar{S} \leq 0.45$ . The theoretical results display strong consistency, thus only the results with two groups of typical data are presented in the following. Here the tube material is 201 stainless steel, and the tube length  $L$  is 50mm.

### 4.2.1 Effects of the vertical semi-axis $b$

The vertical semi-axis  $b$  describes the size of the tube. The force-displacement curves of tubes with various vertical semi-axis  $b$  are shown in Fig. 10(a) and (c), and the energy absorption properties are displayed in Fig. 10(b) and (d). From the results, the tube with larger vertical semi-axis  $b$  has obviously larger energy absorption capacity. However, the mass and the space volume of the tube with larger vertical semi-axis  $b$  is also larger, thus apart from the total energy absorption  $EA$ , the vertical semi-axis  $b$  has a little effect on energy absorption properties. Therefore, in engineering applications, the tube size can be selected according to storage space and manufacturability.

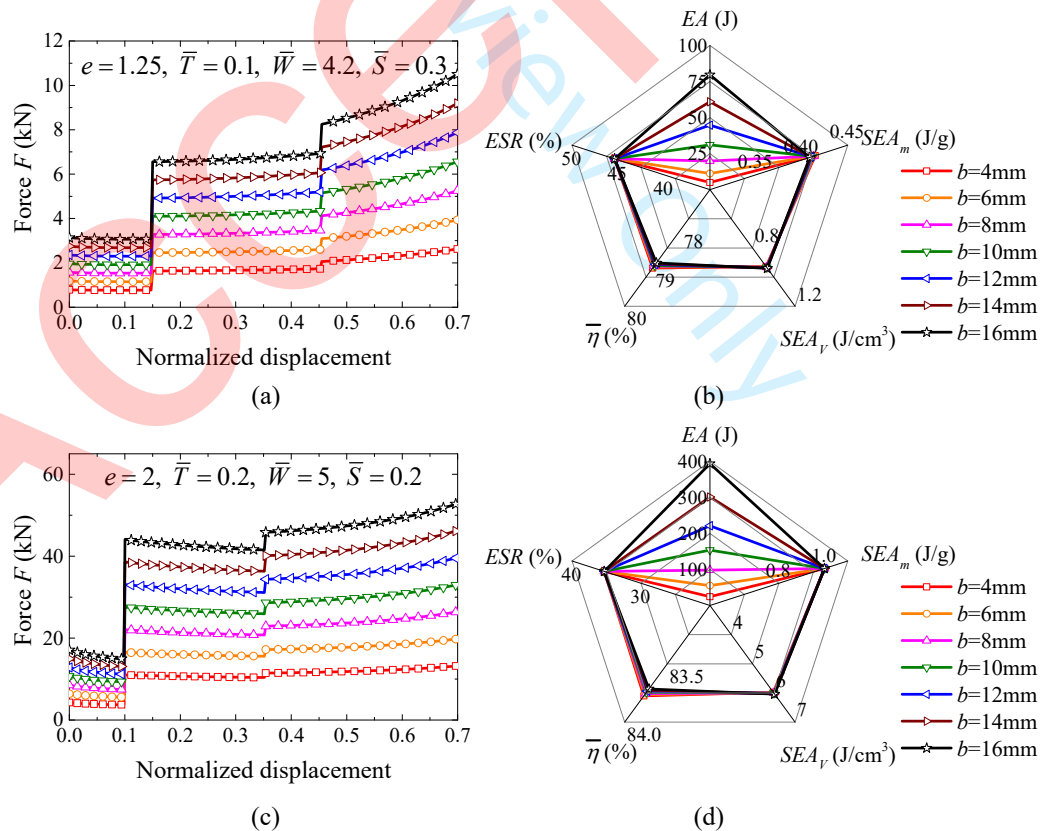


**Fig. 10.** Effects of the vertical semi-axis  $b$  on force-displacement curves and energy

absorption properties with (a) and (b)  $e = 1.25$ ,  $\bar{T} = 0.1$ ,  $\bar{W} = 4.2$ ,  $\bar{S} = 0.3$ ; (c) and (d)

$$e = 2, \bar{T} = 0.2, \bar{W} = 5, \bar{S} = 0.2.$$

#### 4.2.2 Effects of the ovality $e$

The ovality  $e$  determines the shape of the ellipses of the tube. The force-displacement curves of tubes with various ovality  $e$  are shown in Fig. 11(a) and (c), and the energy absorption properties are displayed in Fig. 11(b) and (d). From the results, the tube with larger ovality  $e$  has obviously larger energy absorption capacity, because the ellipse with larger ovality  $e$  has larger stiffness along the compressive direction. As shown in Fig. 11(b) and (d),  $EA$ ,  $SEA_m$  and  $SEA_V$  of the tube all increase with ovality  $e$  obviously. However, the effective stroke ratio  $ESR$  is much limited when  $e$  is large. For energy absorption efficiency, as shown in Fig. 11(b) and (d), the tube efficiency  $\bar{\eta}$  reaches the maximum of about 80% when  $1.5 \leq e \leq 2$ . Taking both energy absorption capacity and efficiency into consideration,  $e_{opt}=2$  is adopted as the optimal design for the tube ovality.

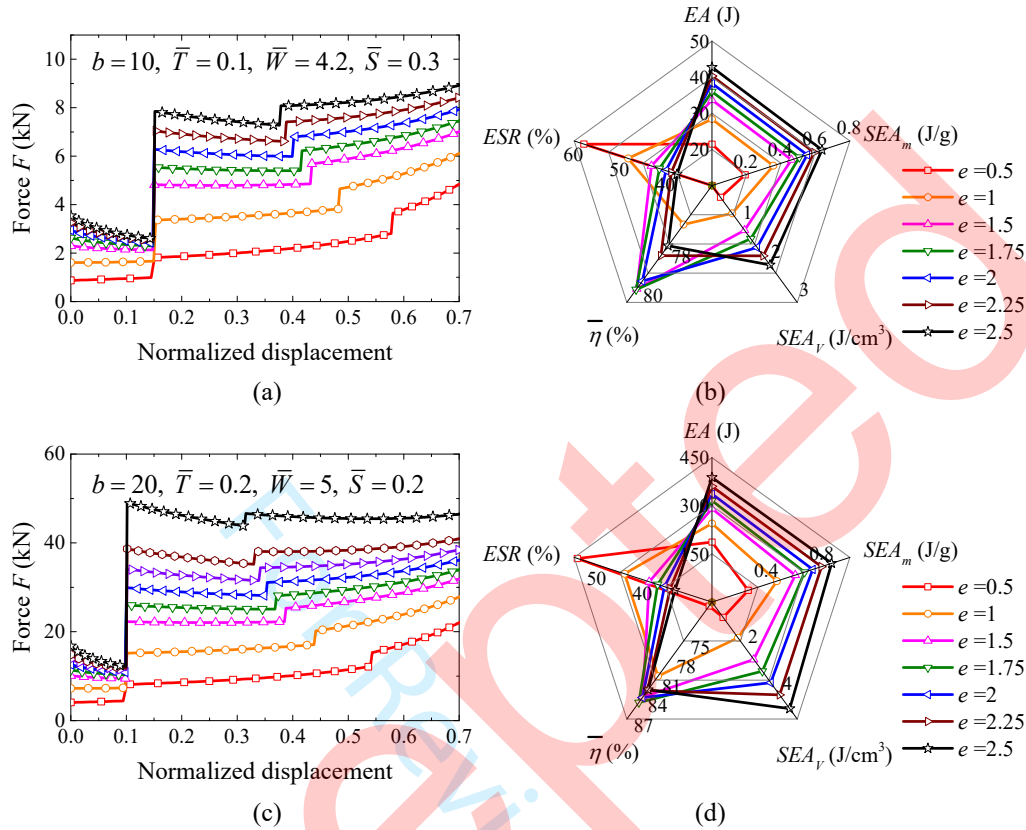


**Fig. 11.** Effects of the ovality  $e$  on force-displacement curves and energy absorption properties with (a) and (b)  $b = 10$ ,  $\bar{T} = 0.1$ ,  $\bar{W} = 4.2$ ,  $\bar{S} = 0.3$ ; (c) and (d)  $b = 20$ ,  $\bar{T} = 0.2$ ,  $\bar{W} = 5$ ,  $\bar{S} = 0.2$ .

#### 4.2.3 Effects of the normalized thickness $\bar{T}$

The effects of the normalized thickness  $\bar{T}$  on force-displacement curves and energy absorption properties are provided in Fig. 12. The tube with larger normalized thickness  $\bar{T}$  has obviously larger energy absorption capacity, and  $EA$ ,  $SEAm$  and  $SEAv$  all increase with the increase of normalized thickness  $\bar{T}$ . However, the maximum force increases more significantly with  $\bar{T}$ , which leads to the decrease in normalized energy absorption efficiency  $\bar{\eta}$ . In addition, the effects of the normalized thickness  $\bar{T}$  on the effective stroke ratio  $ESR$  can be neglected. Therefore, in most

engineering fields, the thickness  $T$  should be selected according to specific protection requirements. Thin-walled tubes are often used for high efficiency, and thick-walled tubes are used for high energy absorption and high specific energy absorption.

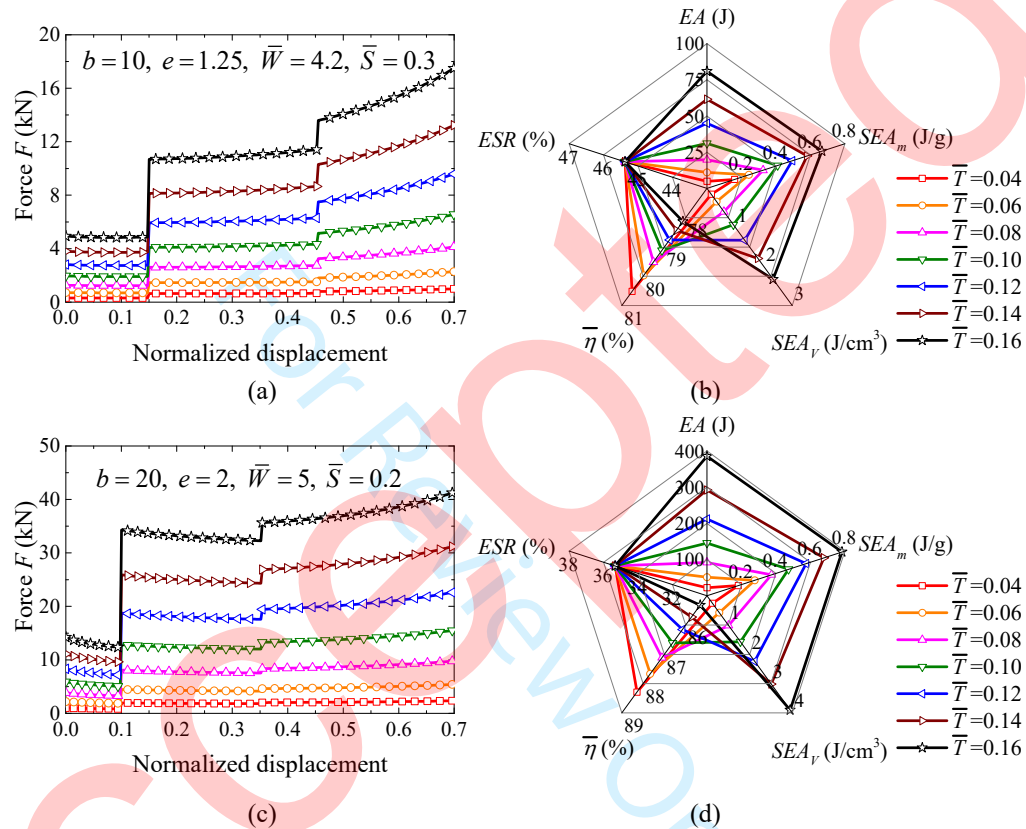


**Fig. 12.** Effects of the normalized thickness  $\bar{T}$  on force-displacement curves and energy absorption properties with (a) and (b)  $b=10, e=1.25, \bar{W}=4.2, \bar{S}=0.3$ ; (c) and (d)  $b=20, e=2, \bar{W}=5, \bar{S}=0.2$ .

#### 4.2.4 Effects of the normalized flat plate width $\bar{W}$

The flat plates of the tube are mainly used to inter-lock the neighboring tubes, and they can hardly affect the force response. However, large normalized flat plate width  $\bar{W}$  leads to the early termination of phase II and accordingly small ESR, as shown in Fig. 13. Therefore, as shown in Fig. 13(b) and (d), all energy absorption

properties increase when decreasing the normalized flat plate width  $\bar{W}$ . According to the requirement of self-locking effect, the flat plate width  $W$  should satisfy  $W \geq 2(2a + T)$  [26]. Therefore, the optimal normalized flat plate width  $\bar{W}_{opt}$  can be expressed as

$$\bar{W}_{opt} = \frac{4}{e} + 2\bar{T} \quad (43)$$

According to the optimal ovality  $e_{opt}=2$  in Section 4.2.2,  $\bar{W}_{opt} = 2 + 2\bar{T}$  is adopted in the optimal design.

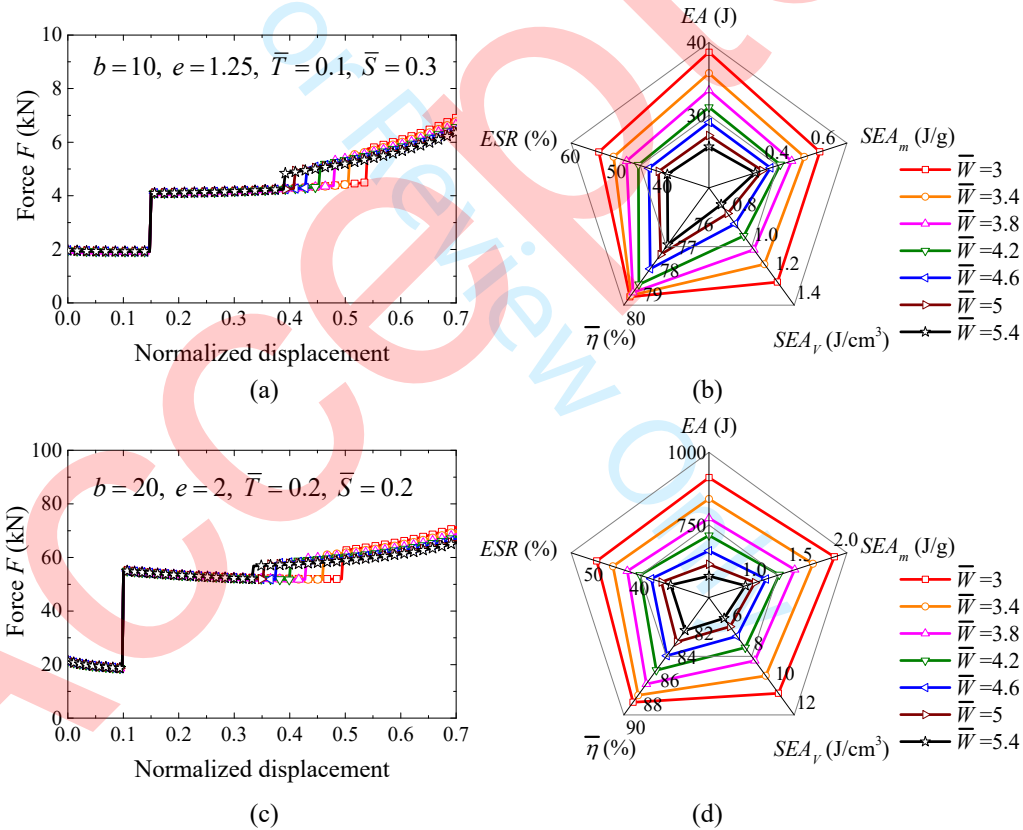


**Fig. 13.** Effects of the normalized flat plate width  $\bar{W}$  on force-displacement curves and energy absorption properties with (a) and (b)  $b = 10, e = 1.25, \bar{T} = 0.1, \bar{S} = 0.3$ ; (c) and (d)  $b = 20, e = 2, \bar{T} = 0.2, \bar{S} = 0.2$ .

#### 4.2.5 Effects of the normalized flat plate spacing $\bar{S}$

According to the analysis on the deformation process in Section 3.2, the plate spacing  $S$  dominates the maximum displacement in Phase I. Tubes with larger normalized flat plate spacing  $\bar{S}$  have larger  $\bar{\delta}_1$ , as shown in Fig. 14(a) and (c). However,  $\bar{S}$  can hardly affect  $\bar{\delta}_{II}$  or force response. As shown in Fig. 14(b) and (d), the effects of  $\bar{S}$  on  $ESR$  can be ignored, but  $EA$ ,  $SEA_m$ ,  $SEA_v$  and  $\bar{\eta}$  all increase when decreasing  $\bar{S}$  due to the decreasing  $\bar{\delta}_1$ . Therefore, the flat plate spacing  $\bar{S}$  should be selected as small as possible if the manufacturability difficulty does not increase significantly.

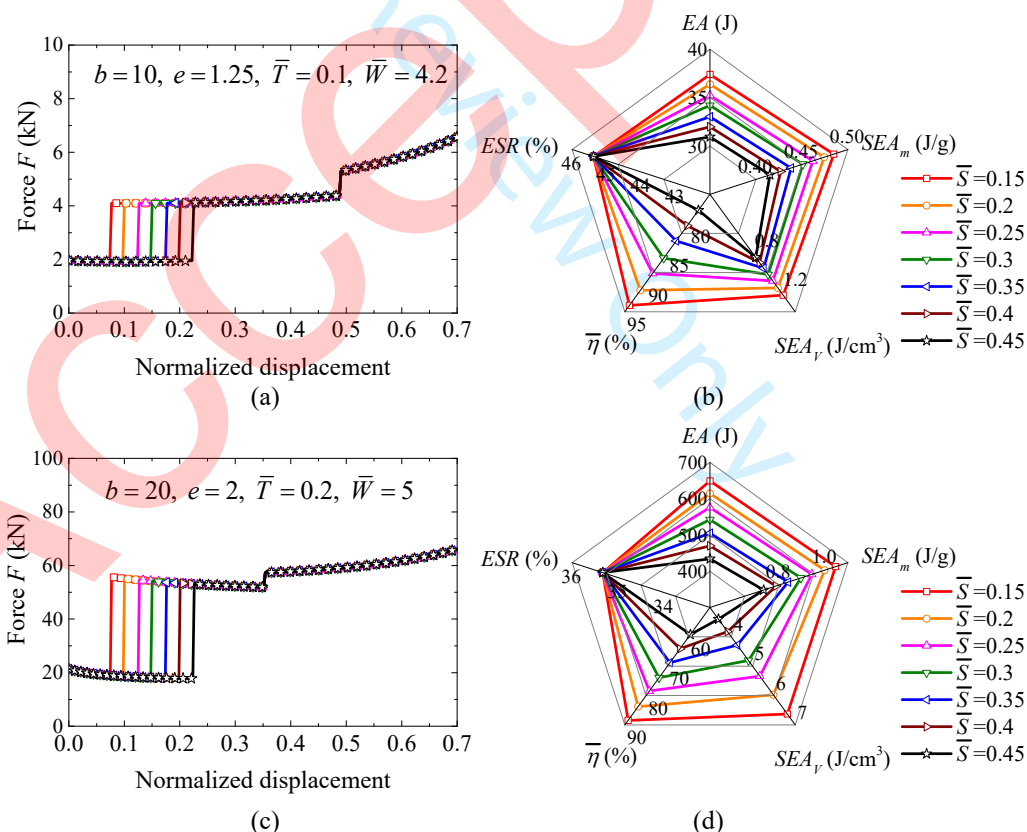


**Fig. 14.** Effects of the normalized flat plate spacing  $\bar{S}$  on force-displacement curves and energy absorption properties with (a) and (b)  $b = 10, e = 1.25, \bar{T} = 0.1, \bar{W} = 4.2$ ;

(c) and (d)  $b = 20$ ,  $e = 2$ ,  $\bar{T} = 0.2$ ,  $\bar{W} = 5$ .

### 4.3 Multiple-tube system

For multiple-tube systems, the deformation of tube flat plates can be limited by adjacent tubes, as shown in Fig. 1(a). Although the constraints of adjacent tubes is ignored in the theoretical analysis in order to achieve an analytical solution, the total energy absorption of the system can be roughly estimated by the single tube energy absorption obtained from the proposed model. To present the applicability of the theoretical model for multiple-tube system, we carried out the FEM simulations of various multiple-tube systems with various tube parameters and total tube number  $n_{\text{total}}$  here. The FEM simulation is conducted by ABAQUS/Explicit, with crushing velocity of 1m/s. The material is adopted as 201 stainless steel, with mechanical parameters provided in Table 3. The geometric parameters are adopted as  $0.5 \leq e \leq 2$ ,  $0.05 \leq \bar{T} \leq 0.2$ ,  $2.1 \leq \bar{W} \leq 8.4$ ,  $\bar{S} = 0.2$ ,  $b = 10\text{mm}$  and  $L = 50\text{mm}$ . The total tube number of the systems  $n_{\text{total}}$  is ranging from 15 to 45. The tube model is modeled using shell element S4R, and the other simulation details are the same as that of Section 2.3. For each system, the total energy absorption at 70% normalized displacement  $EA_{\text{total}}$  is obtained from FEM simulation. In addition, the theoretical energy absorption of single tube  $EA_{\text{single}}$  with same parameters at 70% normalized displacement is calculated based on Eq. (35). The relationship between  $EA_{\text{total}}$  and  $EA_{\text{single}} \cdot n_{\text{total}}$  is depicted in Fig. 15. From the results, the energy absorption of the system  $EA_{\text{total}}$  is approximately proportional to  $EA_{\text{single}} \cdot n_{\text{total}}$ , indicating the geometry effects in Section 4.2 obtained from theoretical model are also instructive and

meaningful to multiple-tube system design. The value of  $EA_{\text{total}}$  is extensively higher than  $EA_{\text{single}} \cdot n_{\text{total}}$ , because the deformation of tube flat plates is limited by adjacent tubes in multiple-tube system, and accordingly, the crushing force increases.

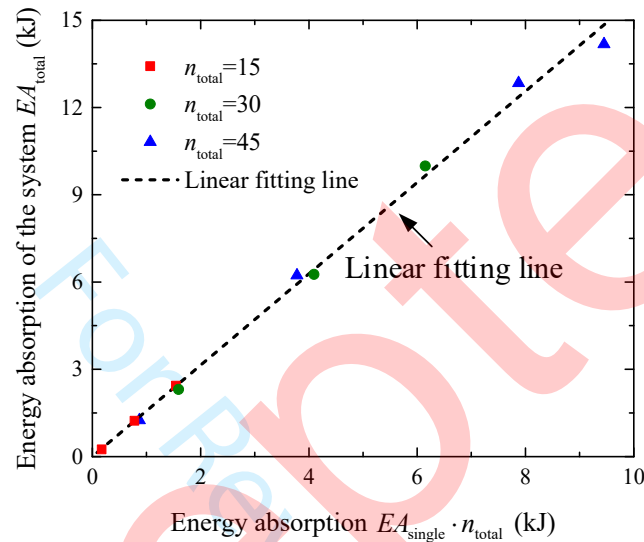


**Fig. 15.** The relationship between the energy absorption of the system  $EA_{\text{total}}$  and the energy absorption  $EA_{\text{single}} \cdot n_{\text{total}}$  in various multiple-tube systems.

#### 4.4 Design of the system

From the above discussion, a guideline on the design of the ellipse-shaped self-locked tube system is provided as below.

- (1) Select the metal with a low prime cost, easy manufacturability and high specific energy absorption as tube material, such as stainless steel or aluminum alloy.
- (2) Estimate the crushing velocity  $v$  and the mass  $M$  of the striking object, and calculate the total energy absorption of the system  $EA_{\text{total}}$  required in applications.
- (3) Select suitable tube length  $L$ , vertical semi-axis  $b$  and total tube number  $n_{\text{total}}$  according to the storage space for the energy absorption system.

- (4) Calculate the horizontal semi-axis  $a$  according to  $e_{opt}=2$ .
- (5) Determine the flat plate width  $W$  according to  $W = 2(2a + T)$ .
- (6) Select a smallest possible flat plate spacing  $S$  according to the manufacturability difficulty.
- (7) Calculate the energy absorption requirement of each tube  $EA_{each}$  in requirement by  $EA_{each} = EA_{total}/n_{total}$ , and investigate the maximum allowable force of the protected objects.
- (8) Select a suitable tube thickness  $T$ , of which the upper bound should meet the requirement of the maximum allowable force and the lower bound should satisfy the lowest energy absorption requirement of each tube.

## 5. Conclusion

A plastic hinge model is established to predict the energy absorption performance of the ellipse-shaped self-locked tube under compression, and the theoretical model is validated by compression experiments and FEM simulations. The following conclusions are drawn from this work.

- (1) The deformation of the tube during the crushing process can be divided into three phases. Phase II dominates the energy absorption, and phase III is the densifying phase.
- (2) The plastic hinge model established in this paper is able to estimate the crushing force and energy absorption properties. The relative error of the tube total energy absorption  $EA$  between the theoretical model and the FEM simulation result is less than 4.2%.

- 1  
2  
3  
4 (3) Increasing the vertical semi-axis  $b$ , the ovality  $e$  and the normalized thickness  $\bar{T}$   
5  
6 can all promote the energy absorption capacity significantly. However, the mass,  
7  
8 space volume and the maximum force  $F_{\max}$  of the tube may also increase. The  
9  
10 vertical semi-axis  $b$  should be determined according to storage space and  
11  
12 manufacturability.  $e_{opt}=2$  is adopted as the optimal design for the tube ovality, and  
13  
14 the optimal thickness  $T_{opt}$  should be selected according to the maximum allowable  
15  
16 force and the lowest requirements of energy absorption properties.  
17  
18  
19  
20  
21 (4) The flat plate width  $W$  and spacing  $S$  display minor effect on energy absorption  
22  
23 properties. The flat plate width  $W$  should be determined by  $\bar{W}_{opt} = 2 + 2\bar{T}$  taking  
24  
25 the self-locking effect requirements into consideration, and the flat plate spacing  
26  
27  $S$  should be set as small as possible provided no manufacturability difficulty is  
28  
29 increased.  
30  
31  
32

### 33 Acknowledgements

34  
35 Supports by the National Natural Science Foundation of China (Nos. 11622214,  
36  
37 11472027 and 11202012), the Academic Excellence Foundation of BUAA for PhD  
38  
39 Students and the Beijing Advanced Discipline Center for Unmanned Aircraft System  
40  
41 are gratefully acknowledged.  
42  
43  
44

### 45 References

- 46  
47 [1] G. Lu, T. Yu. Cambridge: Woodhead Publishing Limited, 385 (2003).  
48 [2] A. A. A. Alghamdi. Thin Wall Struct, **39**, 189 (2001).  
49 [3] W. Abramowicz. Thin Wall Struct, **41**, 91 (2003).  
50 [4] W. Johnson, S. R. Reid. Appl Mech Rev, **31**, 277 (1978).  
51 [5] A. G. Olabi, E. Morris, M. S. J. Hashmi. Thin Wall Struct, **45**, 706 (2008).  
52 [6] P. H. Thornton, R. A. Jeryan. Int J Impact Eng, **7**, 167 (1988).  
53 [7] K. Amini, W. Altenhof, S. C. K. Yuen, C. J. Opperman, G. N. Nurick. Int J  
54  
55 Impact Eng, **110**, 228 (2017).  
56  
57  
58

- 1  
2  
3 [8] A. Baroutaji, M. D. Gilchrist, D. Smyth, A. G. Olabi. *Thin Wall Struct*, **86**, 121  
4 (2015).  
5 [9] K. R. F. Andrews, G. L. England, E. Ghani. *Int J Mech Sci*, **25**, 687 (1983).  
6 [10] J. Li, G. Gao, H. Dong, S. Xie, W. Guan. *Thin Wall Struct*, **103**, 105 (2016).  
7 [11] R. Liu, H. Wang, J. Yang, H. Liu, Y. Sun. *Appl Math Mech-ENGL*, **36**, 1005  
8 (2015).  
9 [12] H. Wang, R. Liu, J. Yang, H. Liu, Y. Sun. *Appl Math Mech*, **37**, 227 (2016).  
10 [13] X. W. Zhang, H. Su, T. X. Yu. *Int J Impact Eng*, **36**, 402 (2009).  
11 [14] C. Y. Wu, L. Y. Li, C. Thornton. *Int J Impact Eng*, **32**, 593 (2005).  
12 [15] G. M. Nagel, D. P. Thambiratnam. *Int J Impact Eng*, **32**, 1595 (2006).  
13 [16] A. Baroutaji, E. Morris, A. G. Olabi. *Thin Wall Struct*, **82**, 262 (2014).  
14 [17] C. Zhou, B. Wang, J. Ma, Z. You. *Int J Mech Sci*, **118**, (2016).  
15 [18] H. Wang, J. Yang, H. Liu, Y. Sun, T. X. Yu. *Thin Wall Struct*, **91**, 72 (2015).  
16 [19] Y. Liu, T. A. Schaedler, X. Chen. *Mech Mater*, **77**, 1 (2014).  
17 [20] Z. Ahmad, D. P. Thambiratnam, A. C. C. Tan. *Int J Impact Eng*, **37**, 475 (2010).  
18 [21] S. Nemat-Nasser, W. J. Kang, J. D. Mcgee, G. W.-G, J. B. Isaacs. *Int J Impact*  
19 *Eng*, **34**, 1119 (2007).  
20 [22] Y. Xiang, M. Wang, T. Yu, L. Yang. *Int J Appl Mech*, **7**, (2015).  
21 [23] E. E. Haro, A. G. Odeshi, J. A. Szpunar. *Int J Impact Eng*, **96**, 11 (2016).  
22 [24] Y. Chen, C. Qiao, X. Qiu, S. Zhao, C. Zhen, B. Liu. *J Mech Phys Solids*, **87**, 130  
23 (2016).  
24 [25] K. Yang, Q. Qin, Z. Zhai, C. Qiao, Y. Chen, J. Yang. *Int J Impact Eng*, **122**, 209  
25 (2018).  
26 [26] K. Yang, Y. Chen, L. Zhang, F. Xiong, X. Hu, C. Qiao. *Int J Mech Sci*, **156**, 312  
27 (2019).  
28 [27] J. A. Deruntz, P. G. Hodge. *J Appl Mech-T ASME*, **30**, (1962).  
29 [28] R. Burton, J. Craig. *BSc (Engineering) Report*, (1963).  
30 [29] S. R. Reid, T. Y. Reddy. *Int J Solids Struct*, **14**, 213 (1978).  
31 [30] C. Qiao, Y. Chen, S. Wang, K. Yang, X. Qiu. *Int J Mech Sci*, **123**, 20 (2017).  
32 [31] N. Qiu, Y. Gao, J. Fang, Z. Feng, G. Sun, Q. Li. *Finite Elem Anal Des*, **104**, 89  
33 (2015).  
34 [32] Y. Xiang, T. Yu, L. Yang. *Mater Design*, **89**, 689 (2016).  
35 [33] K. Yang, Y. Chen, S. Liu, C. Qiao, J. Yang. *Thin Wall Struct*, **119**, 371 (2017).  
36 [34] B. C. Chen, M. Zou, G. M. Liu, J. F. Song, H. X. Wang. *Int J Impact Eng*, **115**,  
37 48 (2018).  
38  
39  
40  
41  
42  
43  
44  
45  
46  
47  
48  
49  
50  
51  
52  
53  
54  
55  
56  
57  
58

# Theoretical investigation on the energy absorption of ellipse-shaped self-locked tubes

Kuijian Yang<sup>1,#</sup>, Chuan Qiao<sup>2,#</sup>, Feng Xiong<sup>1</sup>, Lei Zhang<sup>1</sup>, Zhangming Wu<sup>3</sup>,

Yuli Chen<sup>1,\*</sup>

<sup>1</sup> Institute of Solid Mechanics, Beihang University, Beijing 100191, China

<sup>2</sup> Department of Mechanical Engineering, McGill University, Montreal, QC H3A0C3, Canada

<sup>3</sup> Cardiff School of Engineering, Queens Buildings, The Parade, Newport Road, Cardiff CF24 3AA, UK

#These authors contributed equally to this work.

\* To whom correspondence may be addressed: yulicheng@buaa.edu.cn

## Appendix

**A1. Tensile test for mechanical properties of white photopolymer resin**

**A2. Theoretical model for the rotation of ellipse arc**

**A3. Linear elastic analysis for small deformation**

## A1. Tensile test for mechanical properties of white photopolymer resin

To obtain the mechanical properties of white photopolymer resin, the standard tensile test was conducted according to the test standard ISO 527-1: 1993. The tensile specimen was manufactured by 3D printing made of white photopolymer resin, with thickness of 4mm and cross-sectional view provided in Fig. A.1(a). The tensile test was conducted by test machine MTS 880, and the engineering stress-strain curve is depicted as blue solid curve in Fig. A.1(b). The Young's modulus, initial yield stress and hardening modulus of white photopolymer resin are obtained according to the tension test curve, and listed in Table 1. The bilinear elastic-plastic constitutive model in FEM simulation using these parameters are displayed as red dashed curve in Fig. A.1, which coincides well with the tensile test.

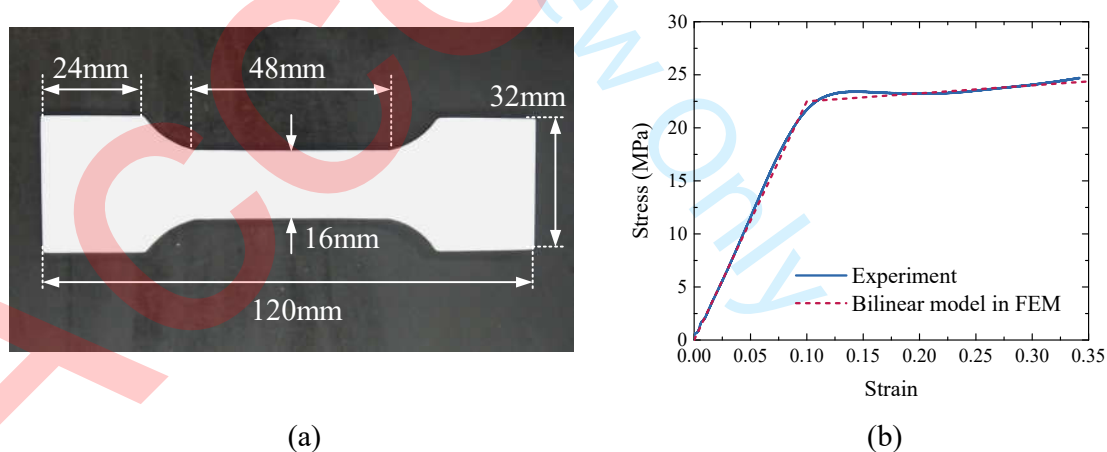


**Fig. A.1.** Tensile test for mechanical properties of white photopolymer resin: (a) experimental specimen and (b) stress-strain curve obtained.

## A2. Theoretical model for the rotation of ellipse arc



$$y = \frac{(1-e^2)\sin\psi\cos\psi}{e^2\sin^2\psi + \cos^2\psi}x + \frac{e\sqrt{a^2(e^2\sin^2\psi + \cos^2\psi) - x^2}}{e^2\sin^2\psi + \cos^2\psi} \quad (\text{A.3})$$

The horizontal coordinate of the critical point D  $x_{D1}$  satisfies

$$y'|_{x=x_{D1}} = 0 \quad (\text{A.4})$$

Substituting Eq. (A.3) into Eq. (A.4), the horizontal coordinate of the critical point D  $x_{D1}$  is calculated as

$$x_{D1} = a(1-e^2)\sin\psi\cos\psi\sqrt{\frac{e^2\sin^2\psi + \cos^2\psi}{(e^2-1)^2\sin^2\psi\cos^2\psi + e^2}} \quad (\text{A.5})$$

Substituting Eq. (A.5) into Eq. (A.3), we obtain the vertical coordinate of the critical point D  $y_{D1}$

$$y_{D1} = a\sqrt{\frac{(e^2-1)^2\sin^2\psi\cos^2\psi + e^2}{e^2\sin^2\psi + \cos^2\psi}} \quad (\text{A.6})$$

After translating the rotated Cartesian coordinate system with a distance  $\Delta(\psi) = (b\sin\psi, -a\sin\psi)$ , the coordinate of the critical point D become

$$x_{D2} = a(1-e^2)\sin\psi\cos\psi\sqrt{\frac{e^2\sin^2\psi + \cos^2\psi}{(e^2-1)^2\sin^2\psi\cos^2\psi + e^2}} + b\sin\psi \quad (\text{A.7})$$

and

$$y_{D2} = a\sqrt{\frac{(e^2-1)^2\sin^2\psi\cos^2\psi + e^2}{e^2\sin^2\psi + \cos^2\psi}} - a\sin\psi \quad (\text{A.8})$$

According to Fig. A.2, the vertical displacement of the loading plate  $\delta$  satisfies

$\delta = b - y_{D2}$ , and accordingly, the normalized displacement  $\bar{\delta}$  can be expressed as

$$\bar{\delta}(\psi) = 1 - \frac{y_{D2}}{b} = 1 + \frac{\sin\psi}{e} - \frac{1}{e}\sqrt{\frac{(e^2-1)^2\sin^2\psi\cos^2\psi + e^2}{e^2\sin^2\psi + \cos^2\psi}} \quad (\text{A.9})$$

The horizontal displacement between points D and C  $p$  can be calculated by

$$p = b\sin\psi + a\cos\psi - x_{D2} \quad (\text{A.10})$$

Substituting Eq. (A.7) into Eq. (A.10), we obtain that

$$p(\psi) = a \cos \psi + a(e^2 - 1) \sin \psi \cos \psi \sqrt{\frac{e^2 \sin^2 \psi + \cos^2 \psi}{(e^2 - 1)^2 \sin^2 \psi \cos^2 \psi + e^2}} \quad (\text{A.11})$$

### A3. Linear elastic analysis for small deformation

In elastic stage, the compression process of the tube can be studied with the linear elastic beam model, as shown in Fig. A.3. Due to symmetry and continuity conditions, an axial force and a moment are acting on points O and C, respectively. Based on global equilibrium, the axial force acting at point O vanishes. The moment acting at point O is defined as  $M_O$ , and the external compressive force locating at point B is defined as  $F_{\text{ela}}$ .

The elastic strain energy of the model in bending can be expressed as

$$U_{\text{tube}} = \int_{\widehat{OAB}} \frac{M_O^2}{2EI} ds + \int_0^{\frac{\pi}{2}} \frac{(M_O - F_{\text{ela}} a \cos \theta)^2}{2EI} \cdot a \sqrt{1 + (e^2 - 1) \cos^2 \theta} d\theta \quad (\text{A.12})$$

where  $E$  is the Young's modulus,  $I = LT^3/12$  is the moment of inertia, and the length of arc  $\widehat{OAB}$  can be approximated as

$$l_{\widehat{OAB}} = \frac{W - S}{2} + \max(a, b) + \frac{\pi - 2}{2} \cdot \min(a, b) \quad (\text{A.13})$$

According to the Castigliano theorem and symmetry, the rotation angle at point O satisfies

$$\frac{dU_{\text{tube}}}{dM_O} = 0 \quad (\text{A.14})$$

From Eqs. (A.12)-(A.14), we obtain that

$$M_O = \frac{(2e^2 + 4)a^2 F_{\text{ela}}}{3 \left[ W - S + 2 \max(a, b) + (\pi - 2) \min(a, b) + \frac{\pi a (e^2 + 3)}{4} \right]} \quad (\text{A.15})$$

The compression displacement  $\delta$  of the loading plate with respect to the horizontal

symmetry plane satisfies

$$\delta = \frac{dU_{\text{tube}}}{dF_{\text{ela}}} \quad (\text{A.16})$$

From Eqs. (A.12)-(A.16), the external force acting on this model can be expressed as

$$F_{\text{ela}} = \frac{EL\bar{T}^3 e^4 a \bar{\delta}}{\frac{9e^2 + 15}{8} \pi - \frac{8(e^2 + 2)^2}{3 \left[ e(\bar{W} - \bar{S}) + 2 \max(1, e) + (\pi - 2) \min(1, e) + \frac{\pi(e^2 + 3)}{4} \right]}} \quad (\text{A.17})$$

Based on Eq. (A.17), the force-displacement curves of the tubes obtained from linear elastic solution are presented in Fig. 9, with mechanical properties listed in Table 3 and geometric parameters provided in Table 4. From the results, the elastic solution in Eq. (A.17) coincides well with the simulation results at the beginning of the crushing process. With the development of the compression, the crushing is no longer dominated by the elastic deformation, and accordingly, the elastic solution is no longer proper for this problem and a plastic analysis is in great demand.

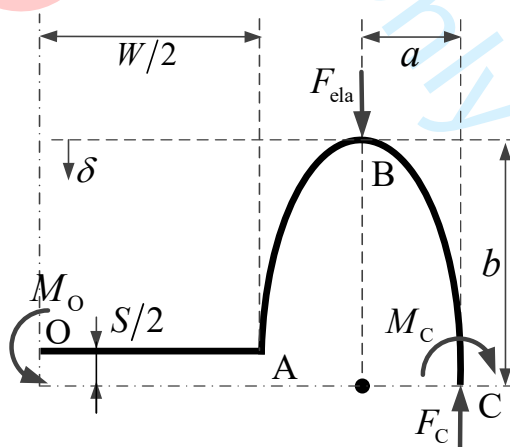


**Fig. A.3.** Linear elastic beam model of the tube at small deformation.